FACULTY
OF MATHEMATICS
AND PHYSICS
Charles University

BACHELOR THESIS

Filip Hájek

Preparation and characterization of Lu$_2$Ir$_2$O$_7$ single crystals

Department of Condensed Matter Physics

Supervisor of the bachelor thesis: RNDr. Milan Klicpera, Ph.D.

Study programme: Fyzika

Study branch: Fyzika Bc.

Prague 2023

I declare that I carried out this bachelor thesis independently, and only with the cited sources, literature and other professional sources. It has not been used to obtain another or the same degree.

I understand that my work relates to the rights and obligations under the Act No. 121/2000 Sb., the Copyright Act, as amended, in particular the fact that the Charles University has the right to conclude a license agreement on the use of this work as a school work pursuant to Section 60 subsection 1 of the Copyright Act.

In . . . . date . . . .

Author's signature

Title: Preparation and characterization of $Lu_2Ir_2O_7$ single crystals

Author: Filip Hájek

Department: Department of Condensed Matter Physics

Supervisor: RNDr. Milan Klicpera, Ph.D., Department of Condensed Matter Physics

Abstract: Present thesis is focused on the synthesis and characterization of $Lu_2Ir_2O_7$ single crystals as a part of a broader study of rare-earth $A_2Ir_2O_7$ pyrochlore iridates, where A = Y, La-Lu. These materials, crystallizing in the geometrically frustrated pyrochlore lattice and with electronic properties being shaped by strong spin-orbit interaction, have attracted considerable attention of the condensed matter community. The investigation of $Lu_2Ir_2O_7$ with nonmagnetic Lu^{3+} cations is crucial in order to reveal the physical properties connected to magnetism of solely the Ir sublattice. The physical properties connected to the Ir sublattice are essential for a proper interpretation of the complex properties of other $A_2Ir_2O_7$ with magnetic rare-earth cations. For the first time, large good-quality $Lu_2Ir_2O_7$ single crystals were synthesized by means of the flux method. Their stoichiometry and crystal structure were characterized by means of Laue diffraction and energy-dispersive X-ray technique. Magnetic properties were investigated employing magnetization measurements under ZFC and FC regimes. A bifurcation between ZFC and FC magnetizations was revealed at $T_{Ir} = 130(1)$ K, indicating magnetic ordering of the Ir sublattice. Investigating single crystals, the anisotropy effects were studied for the first time. Significantly lower magnetization was observed for magnetic field applied along the [111] crystallographic direction compared to the directions [100] and [110]. The measured data were interpreted considering antiferromagnetic all-in-all-out ordering of Ir magnetic moments and hypothesized formation of field-oriented domains and ferromagnetic domain walls below T_{Ir}. The results were discussed in the framework of previous studies on $A_2Ir_2O_7$ pyrochlores and $Lu_2Ir_2O_7$ polycrystal.

Keywords: single crystals, pyrochlore structure, structure and phase characterization

Název práce: Příprava a charakterizace monokrystalů $Lu_2Ir_2O_7$

Autor: Filip Hájek

Katedra: Katedra fyziky kondenzovaných látek

Vedoucí bakalářské práce: RNDr. Milan Klicpera, Katedra fyziky kondenzovaných látek

Abstrakt: Tato práce je zaměřena na syntézu a charakterizaci monokrystalů $Lu_2Ir_2O_7$ jako součást širšího výzkumu vzácnozeminných $A_2Ir_2O_7$ pyrochlor iridátů, kde A = Y, La-Lu. Tyto materiály, krystalizující v geometricky frustrované pyrochlorové mříži a s elektronovými vlastnostmi určenými silnou spin-orbitální interakcí, přitahují značnou pozornost vědecké komunity kondenzovaných látek. Studium $Lu_2Ir_2O_7$ s nemagnetickými Lu^{3+} kationty je zásadní pro interpretaci fyzikálních vlastností spojených s magnetismem samotné Ir podmříže. Tyto fyzikální vlastnosti jsou esenciální pro správnou interpretaci komplexních vlastností ostatních $A_2Ir_2O_7$ s magnetickými vzácnozeminnými kationty. Poprvé jsou syntetizovány velké, kvalitní $Lu_2Ir_2O_7$ monokrystaly za použitý metody fluxu. Jejich stechiometrie a krystalová struktura byly charakterizovány za použití Laueho difrakce a energiově-disperzní rentgenové techniky. Magnetické vlastnosti byly zkoumány měřením magnetizace v ZFC a FC režimu. Rozštěpení ZFC a FC magnetizace bylo pozorováno při T_{Ir} = 130(1) K, což naznačuje magnetické uspořádání Ir podmříže. Studium monokrystalů umožnilo poprvé vyšetřovat anisotropické vlastnosti materiálu. Podstatně menší magnetizace byla pozorována pro magnetické pole aplikované v krystalografickém směru [111] v porovnání se směry [100] a [110]. Měřená data byla interpretována s ohledem na antiferomagnetické all-in-all-out uspořádání Ir magnetických momentů a předpokládanou formaci domén orientovaných ve směru přiloženého pole s feromagnetickými rozhraními mezi doménami při teplotách nižších než T_{Ir}. Výsledky byly diskutovány v rámci předchozích studií $A_2Ir_2O_7$ pyrochlorů a $Lu_2Ir_2O_7$ polykrystalu.

Klíčová slova: monokrystaly, pyrochlorová struktura, strukturní a fázová charakterizace

Contents

Introduction

In recent years, $A_2B_2O_7$ oxides, where A represents a rare-earth element and B a d transition metal ($3d$, $4d$ or $5d$ elements) or a p element, have become a subject of major interest in the solid state physics community. Their complex properties involving complicated magnetic ordering, spin ices, spin liquids [1], topological states etc. arise from the interplay between their crystal structure, electron configurations of the A^{3+} and B^{4+} ions, spin-orbit coupling or crystal field.

In the present thesis, we are going to synthesize and study an important member of the pyrochlore iridate ($B = $ Ir) family, $Lu_2Ir_2O_7$ with non-magnetic Lu^{3+} cations. Our thesis serves as a continuation of a research project on the subject of $A_2Ir_2O_7$ synthesis and characterization, conducted at the Charles University's Department of Condensed Matter Physics (DCMP). The previous research, lead by the supervisor of this thesis, RNDr. Milan Klicpera, Ph.D., focused on polycrystalline (powder) samples of these compounds, their synthesis and characterization [2]. Synthesis of $Lu_2Ir_2O_7$ single crystals and their characterization represent a major step forward in the study of the $A_2Ir_2O_7$ family. First, the study of single crystals allows us to determine anisotropic properties of compounds, which is crucial for proper understanding of observed properties, their theoretical description, as well as any future technical applications. Second, the A^{3+} and B^{4+} ions form a complex system of various exchange interactions and magnetic structures. The non-magnetic Lu allows us to isolate properties arising from the Ir sublattice, which can then explain more complex properties of other $A_2Ir_2O_7$.

The present work consists of four chapters. in Chapter 1, we are going to introduce the basis of magnetism and its consequences on the behavior of electrons in materials. Often cited as a prime example of a frustrated system, the pyrochlore structure, crystal structure of the studied iridates, introduces the so-called geometrical frustration due to the corner-sharing tetrahedra formed by both the A and Ir ions. Together with the plethora of possible interactions, e.g. spin-orbit coupling and electron correlations, the iridates form complex systems.

While certain $A_2B_2O_7$ oxides have been thoroughly studied, in the case of the iridates one encounters the problem of single crystal synthesis. Previous studies conducted on the $A_2Ir_2O_7$ oxides have used polycrystalline samples or off-stochiometric single crystals, leaving room for improvement. In Chapter 2,

we are going to describde the flux method implemented to synthesize $A_2\text{Ir}_2\text{O}_7$ single crystals. Moreover, the experimental methods utilized to characterize the prepared samples will be described.

In Chapter 3, we are going to discuss general findings previously published by the solid state physics community. We will establish some general ideas related to competing interactions, phase transitions and the resulting exotic phases.

After outlining general features of the $A_2\text{Ir}_2\text{O}_7$ members, we are going to focus on obtained results in Chapter 4. We will specify the setup and conditions of the $\text{Lu}_2\text{Ir}_2\text{O}_7$ synthesis by flux method, which resulted in stoichiometric single crystals of maximum size between 100-500 μm. The structure and chemical composition analysis by means of Laue diffraction and EDX will be discussed. We will then analyze the measurements of magnetization response to an external magnetic field and temperature in the synthesized $\text{Lu}_2\text{Ir}_2\text{O}_7$ single crystals. These measurements allowed us to determine the temperature T_{Ir}, at which the Ir sublattice magneticaly orders, the magnetic moment value on Ir ions and its evolution with temperature, as well as clear differences in magnetization measured on the sample cooled through T_{Ir} under different magnetic field-temperature regimes.

The data are discussed in the framework of previous results on $\text{Lu}_2\text{Ir}_2\text{O}_7$ polycrystal, other $A_2\text{Ir}_2\text{O}_7$ compounds and considering the hypothesis on antiferromagnetic domains and interfaces formation. The main results are summarized in Conclusions, where also future work on $\text{Lu}_2\text{Ir}_2\text{O}_7$ and $A_2\text{Ir}_2\text{O}_7$ single crystals is delineated.

1. Theoretical Background

1.1   Magnetism

Magnetization of a material can be defined in the following way. First, we consider a current loop with current density $\vec{j}(\vec{r}')$, forming the boundary of a surface $\boldsymbol{\Sigma}$, which when integrated over the volume of the loop gives the current I. The current density generates a magnetic field described by the magnetic induction $\vec{B}(\vec{r})$ and its vector potential $\vec{A}(\vec{r})$ related by $\vec{B} = \text{rot}\,\vec{A}$.

If we consider positions $\vec{r}$ far away from the source of $\vec{A}$ i.e. $r \gg r'$, we can write the vector potential as [3]:

$$\vec{A}(\vec{r}) \doteq \frac{\mu_0}{4\pi} I \frac{\vec{\sigma} \times \vec{R}}{R^3} = \frac{\mu_0}{4\pi} \frac{\vec{\mu} \times \vec{R}}{R^3}, \; \vec{\mu} = I\vec{\sigma}, \tag{1.1}$$

where $\vec{R} = \vec{r} - \vec{r}' \doteq \vec{r}$ directs from a given point in the loop to a point in space, $\vec{\sigma}$ is the normal of the surface $\boldsymbol{\Sigma}$ with magnitude corresponding to the surface area of $\boldsymbol{\Sigma}$ and μ_0 is the vacuum magnetic permeability. The magnetic moment of a current loop $\vec{\mu}$ can be generalised as

$$\vec{\mu} = \int_{V'} [\vec{r}' \times \vec{j}(\vec{r}')]\, dV'. \tag{1.2}$$

Finally, for spatially distributed magnetic dipoles in a volume V with a total magnetic moment $\vec{\mu}_V$, we define magnetization $\vec{M}$ by the relation

$$\vec{\mu}_V = \int_V \vec{M}(\vec{r}')\, dV' \tag{1.3}$$

The magnetization $\vec{M}$ of a system of current loops corresponds to the volume density of its magnetic moments.

Depending on the response of the system to an external magnetic field, two general groups of magnetic materials are defined [4]: materials with weak and strong response.

For weakly responding magnetic materials, that is, paramagnets and diamagnets with small $\left|\vec{M}\right|$, we can write

$$\vec{M}(\vec{r}) = \chi\vec{H}(\vec{r}), \tag{1.4}$$

where $\vec{H}$ is the total intensity of the magnetic field and χ is the magnetic sus-

ceptibility of the material. Generally, χ is a dimensionless constant of value $10^{-6} < |\chi| < 10^{-3}$ for weakly magnetic materials. For diamagnetic materials, $\chi < 0$ indicates that the magnetic moments of the ions in the material tend to align opposite to the external field. Paramagnetic materials have $\chi > 0$ and therefore the magnetic moments of ions align along the direction of the external field, add to it, and consequently increase the total field.

Strong magnetic materials are illustrated by ferromagnetic systems, where the dependence $\vec{M}(\vec{H})$ gets more complicated. Compared to diamagnetic and paramagnetic materials, alignment of the magnetic moments in ferromagnets can generate a field that is even stronger than the external field [4]. The magnetization of ferromagnets depends on the temperature-field history of the material (hysteresis loop), which is not the case for paramagnets and diamagnets. Moreover, ferromegnets reveal spontaneous magnetization below critical temperature T_c.

Contrary to ferromagnets, where the magnetic moments align in such a way that they create a strong magnetic field, antiferromagnets are formed by alternating magnetic moments which compensate. The net magnetic moment of an antiferromagnet is thus zero.

To understand the formation of ferromagnets and antiferromagnets, the concept of a magnetic moment is introduced. The magnetic moment of an ion is dictated by the angular momenta of its electrons, which are superimposed based on the laws of quantum mechanics. For a general angular momentum $\vec{J}$, we can write its contribution to the magnetic moment as:

$$\vec{\mu} = -g\frac{e}{2m}\vec{J} = -g\frac{\mu_B}{\hbar}\vec{J}, \tag{1.5}$$

where e is the elemental charge of an electron, m is the electron mass, g is the Landé factor, which is a dimensionless factor characteristic of a given atomic state and $\mu_B = e\hbar/2m$ is the Bohr magneton. Further information can be found, e.g., in [5].

Magnetic moments of individual ions in the crystal lattice interact with each other. Various exchange interactions can be realized, including direct exchange, superexchange, double-exchange, RKKY interaction, and a number of other, usually weaker, interactions [5]. Depending on the interatomic distances between magnetic ions in the crystallographic lattice, crystal field generated by surrounding ions, and inner properties of these ions, including spin-orbit coupling (SOC;

interaction between electron's spin and angular momentum) effects, the material orders magnetically below a characteristic temperature.

1.2   Spin-orbit Coupling

Spin-orbit coupling plays a significant role in the formation of physical, electronic and magnetic properties of the material. SOC is a relativistic (or fine structure) phenomenon, therefore becomes stronger with increasing atomic number Z. Its contribution is usually small in $3d$-elements, however, increases as Z^4 and therefore plays a crucial role in $4d$ and especially $5d$ elements [1].

SOC is the direct consequence of conservation of total angular momentum $\vec{J} = \vec{L} + \vec{S}$. The hamiltonian term describing SOC, with λ being a coefficient defined by the given atomic state, is written as [5]:

$$H_{SOC} = \lambda \vec{S} \cdot \vec{L} \tag{1.6}$$

When considering systems of multiple atoms with multiple electrons, the SOC term is simply the sum of each of the atom's terms with $\vec{S}$ and $\vec{L}$ being the spin and orbital momentum of the given atom.

Strong SOC lifts orbital degeneracy (splits orbital energy levels/multiplets) and entangles the spin and orbital degrees of freedom. In some materials, this causes the reduction of the Fermi level width by which, in combination with the crystal field effects, a Mott insulator state may be induced [1]. Together with electron correlations in the material, another energy level splitting occurs and a wider variety of exotic states may be induced [1, 6].

1.3   Geometrical Frustration

In a solid material with crystalline structure, atoms are bound to each other in a periodic array. Periodic arrays are modeled by crystallographic lattices, defined by a space lattice, reduceable to an elementary lattice, and an atom basis. The combination of the crystal's geometry and the inter-atomic interactions of the basis gives rise to the properties of the crystal [7].

Among crystallographic lattices, geometrically frustrated lattices attract considerable attention of the scientific community. Due to distances between several magnetic ions being the same/similar in specific frustrated lattices, the exchange
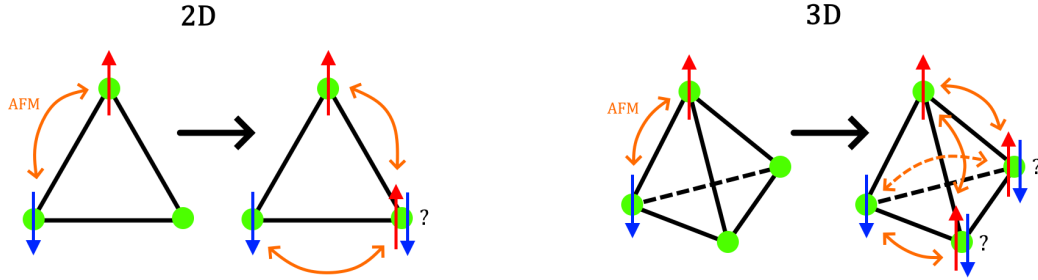
Figure 1.1: Principle of 2D and 3D geometrical frustration, equilateral triangle (2D) and tetrahedron (3D) with dominant antiferromagnetic (AFM) interaction between Ising moments pointing up or down.

interactions between magnetic moments cannot be simultaneously satisfied. Typical example is an equilateral triangle with magnetic ions on its vertices, shown in Figure 1.1. Consider the exchange interactions between moments prefer antiferromagnetic ordering and Ising type of moments. Two of the moments line up accordingly, that is, one is pointing up and the second one pointing down. Third moment cannot satisfy both antiferromagnetic interactions: being simultaneously pointing down (opposite to first moment) and up (opposite to second moment). Of course, the same frustration is applied for all moments on the triangle and in the lattice.

2D geometrically frustrated lattices include, e.g., triangular lattice with edge-sharing triangles, kagomé lattice with corner-sharing triangles, square lattice with two non-equivalent antiferromagnetic pathways (along square edge and diagonal), or so-called Shastry-Sutherland lattice [5, 8].

There are also 3D geometrically frustrated lattices, namely prominent, hyper-kagomé lattice formed by corner-sharing triangles (not in plane, but in space) and pyrochlore lattice of corner-sharing tetrahedra. Consider four magnetic ions at the vertices of a tetrahedron with antiferromagnetically coupled Ising moments. Two moments align antiferromagnetically, however the other two moments cannot couple antiferromagnetically to both of them (and with each other) - Figure 1.1.

In reality the interactions between atoms are more complicated: Several competing interactions may be present, as well as fluctuations due to external variables, e.g., temperature or magnetic field. Focusing on the pyrochlore lattice, lattice of compounds investigated in present thesis, in tetrahedron, the principal axis usually corresponds to the local $\langle 111 \rangle$ axis [1]. Magnetic moments align along this axis, frequently forming either antiferromagnetic or ferromagnetic structures, see Figure 1.2. In the case of prevalent antiferromagnetic interactions, the so-called
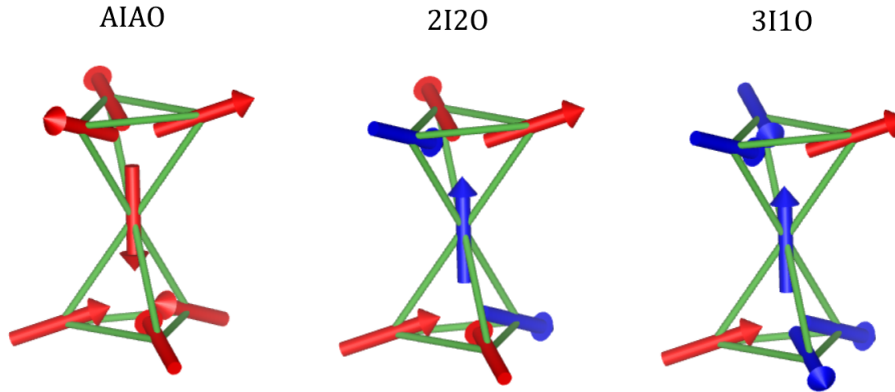
Figure 1.2: The three main configurations of magnetic moments along the local $\langle 111 \rangle$ axis in a tetrahedron (pyrochlore lattice).

all-in-all-out (AIAO) configuration of magnetic moments is realized. Moments at one tetrahedron point all in and in the neighbouring tetrahedra all moments point out. Net magnetic moment is zero, as expected for antiferromagnets. When the prevalent interactions are ferromagnetic, the configurations 2-in-2-out (2I2O) or 3-in-1-out (3I1O) are realized, leading to a non-zero net magnetic moment.

1.4 Thermodynamics of Phase Transitions

Nowadays, crystals are being prepared using numerous methods utilizing our knowledge on phase transitions in matter summarized in the theory of thermodynamics, e.g. [9]. Thermodynamics allow us to describe phase transitions in materials using five thermodynamical potentials and a state of equilibrium (time-independent state), which is reached by minimizing one of the said potentials [9].

When dealing with chemical reactions, it is useful to define the Gibbs free energy $G(T, p)$ using the system's internal energy E, temperature T, pressure p, entropy S and volume V:

$$G(T, p) = E - TS + pV. \tag{1.7}$$

The use of G is beneficial, since experimental conditions are generally defined by temperature and pressure. Thus for a given pressure p, equilibrium is reached by finding the minimum of G as a function of temperature [9].

Thermodynamic behavior varies for every material, thus different methods need to be implemented. A wide diversity of methods allow synthesis of various crystal sizes and phases (polycrystals, single crystals), each useful for certain

applications. Among the main deciding factors for the choice of a method of synthesis are the stability of growth and melting temperature.

For a material with stable growth, the Czochralski and floating zone methods are often used. The Czochralski method is one of the most prominent methods, especially in the semi-conductor industry, where it is used to prepare high quality sillicone crystals. A polycrystalline material is melted in a crucible and a precursor is then pulled out of the melt. A single crystal forms at the connection with the melt. This method allows, depending on the growing conditions, the synthesis of crystals of up to several cm. In contrary, the floating zone method allows melting the precursor while the melt is stabilized by surface tension. The precursor is pulled through a hot zone resulting in a single crystal. The floating zone method is frequently used for the synthesis of, e.g., $A_2B_2O_7$ single crystals [10]. Further information can be found in [7] or [11].

For some materials, methods including a reaction-mediating agent or special conditions need to be implemented. Czochralski, floating zone and other frequently used methods do not allow the synthesis of incongruent materials, materials with volatile elements, complex phase diagrams etc. One of the methods used for synthesis of single crystals of such materials is the flux method (described in section 2.1). Also, the straight forward solid-state-reaction method is frequently used. This method consists of preparing a homogenous mixture of reactants which is then thermally treated while often intermediately ground to reach the best possible homogenity [6]. Another method is the hydrothermal synthesis, where an aqueous mineralization agent is included in the heating process, allowing higher solubility and ion mobility of the reactants. These methods are also often used for $A_2B_2O_7$ single crystal synthesis, e.g. [10] and references therein.

2. Experimental methods

2.1 Flux Method Synthesis

The flux method of material/single crystal synthesis uses an inorganic material, called flux, to mediate the reaction between reactants in the initial precursor/mixture. The flux, a solid material at room temperature, is required to have a melting temperature lower than the desired single crystal. Many materials can be used as a flux, including those being part of the initial mixture and synthesized crystals [6].

Initial materials, pure elements, oxide, nitrades, etc., are properly mixed with the appropriate flux. Whole mixture is heated to a temperature higher than the melting temperature of the flux. The initial material partially/completely dissolves into the flux, which then mediates the formation of single crystals and protects the material from evaporation [10]. As the material dissolves and diffuses in the melted flux, the solution becomes supersaturated and the nucleation process takes place. Upon cooling, the products are stabilized and the flux solidifies as well. In case the flux is removable by water or acids, the mixture can be cooled down to room temperature and processed later. However, in some cases, separation of the flux and products of the synthesis is preferably done before final cooling; that is, before the flux solidifies. Usually, centrifugation of the flux is done.

For sample synthesis by the flux method it is crucial to choose, besides a proper flux, a proper heating profile, i.e. the maximum temperature, reaction time and speed of cooling of the mixture. These factors strongly influence the phase purity and size of the synthesized crystals [6].

2.2 Laue Diffraction

Laue diffraction is a method of crystal structure measurement and analysis which uses diffraction of polychromatic X-ray or neutron radiation (wavelengths usually range from about 0.1 to several Å, i.e. corresponding to/lower than interatomic distances).

Laue diffraction conditions are introduced:

$$\vec{q} = \vec{B}_{hkl} = h\vec{b}_1 + k\vec{b}_2 + l\vec{b}_3 \tag{2.1}$$
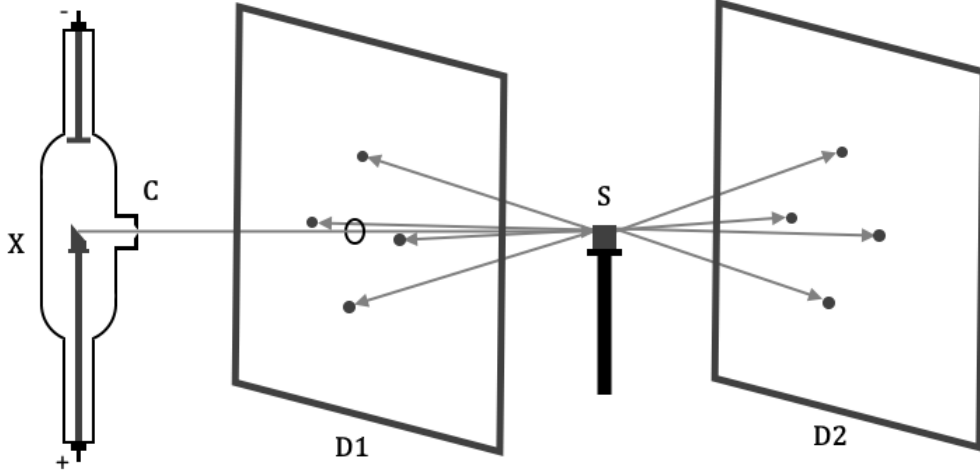
Figure 2.1: Diagram of Laue method/diffraction, X - X-ray source; C - collimator; S - single crystal sample; D1, D2 - detector.

where $\vec{q}$ is the scattering vector, $\vec{b}_{1,2,3}$ are the basis vectors of the reciprocal lattice and h, k and l are the Miller indices (hkl) [7]. For a given wavelength, only specific crystallographic planes can participate in diffraction. Using polychromatic radiation, many planes satisfy the diffraction condition, leading to maps of diffractions, creating the so-called Lauegram. Lauegram shows the part of the reciprocal space containing lattice diffractions and therefore information about lattice symmetries and parameters.

For purposes of present thesis, we used the laboratory Laue diffractometer (for technical specifications see `https://mgml.eu/laboratories/instruments/laue`) at the MGML (Materials Growth and Measurement Laboratory). Diagram of the setup is plotted in Figure 2.1. X-ray source produces radiation - electrons (from thermoemission) are accelerated by a voltage between an anode and a cathode in an evacuated tube, and upon reaching the anode, photoemission of X-ray radiation occurs. Emitted photons pass through a collimator and reach the sample. Crystallographic planes in diffraction condition scatter the photons, and diffracted photons are detected on CCD detectors. Light can be scattered either in the direction of the beam - detection at D2, or scattered back - detection at D1. Measured difractograms contain equivalent information, thus usually only one of the possibilities is used. In the case of the Laue diffractometer used in the present work, backscattered photons were detected, leading to a Lauegram formed by hyperbolas.

2.3   EDX Analysis

Energy-dispersive X-ray (EDX) spectroscopy is a method utilizing X-ray emission analysis to determine the composition of a given material. The EDX setup is frequently included in the scanning electron microscope (SEM) which uses interaction of electrons with matter for imaging, qualitative analysis (morphology of a surface) and quantitative analysis (chemical composition of a material) [7].

SEM used in present work was the TESCAN Mira I LMH and diagram of its setup is drawn in Figure 2.2. Primary electrons (PE) are accelerated by a voltage of 30 kV and processed by the electron optical elements AP, CL, OL into a tight beam that is periodically deviated by the scanning coils SC. An important part of the setup is the distance between the sample (S) and the objective lense (OL) called the working distance (WD). Upon reaching the sample, PE interact with the material and several processes occur, leading to re-emission of three types of electrons and two types of radiation. Due to the strong interaction of electrons with matter because of their charge, the maximum depth of penetration is in the units of μm.

Upon entering the material, at depths of $\sim$nm, the first type of electrons is generated - the Auger electrons, which are emitted when an electron falls to a lower energy level to fill a vacancy and instead of emitting a photon, transferes the remaining energy to another electron and forces said electron to leave the shell. Their energy is usually in the range of 100-1000 eV. At depths of 5-50 nm, the secondary electrons (SE) are generated as a result of ionisation, where an electron scatters inelasticly, transfering its energy to an electron in an atom's shell and forcing it to leave the shell. Secondary electrons usually carry energies of $\sim$50 eV. Lastly, at depths of $\sim \mu$m, back scattered electrons (BSE) are generated by redirection of primary electrons due to the atomic potentials. Their energies can go up to the primary electrons' energy [7].

Since BSE are generated by atomic potentials, the amout of detected BSE depends on the atomic number Z. This fact is what allows us to create an image of a sample's surface. The detected relative intensity is higher for heavier elements and lower for lighter elements, resulting in the so-called composition contrast. Detection is performed by scintilators, which are excited by electrons and upon deexcitation emit a photon, which is in turn transformed into an image.

As a byproduct of the processes generating BSE and SE, X-ray radiation is emitted. Energy (wavelenght) spectrum of X-ray radiation has two main parts
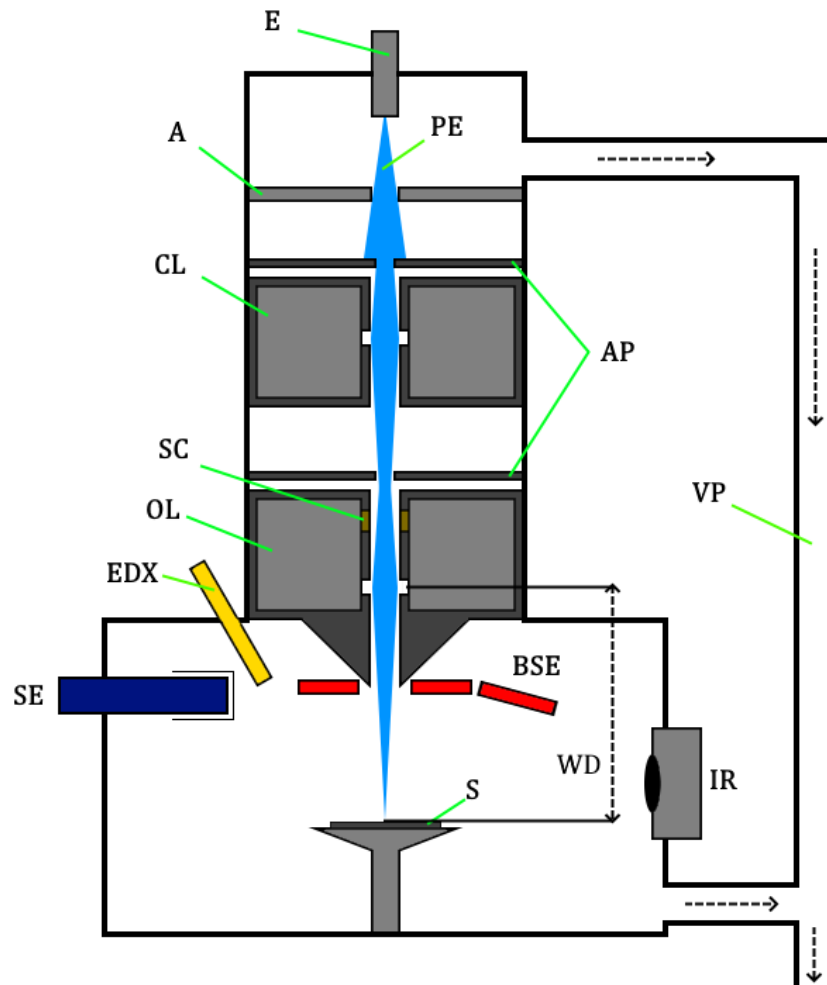
Figure 2.2: Diagram of SEM (Scanning Electron Microscope) TESCAN Mira I LMH. E - source of electrons; PE - primary electron beam; A - anode; AP - aperture; CL - condenser lense; SC - scanning coils; OL - objective lense; EDX - EDX detector; BSE - back scattered electron detector; SE - secondary electron detector; IR - infrared camera; VP - vacuum pump; S - sample; WD - working distance.

- a continuos part and a discrete part. When electrons pass by an atom and are redirected by its electric potential, they experience a centrifugal force and by Newton's law have non-zero accaleration, which means their energy changes. Since energy has to be conserved, they emit photons called braking radiation (bremsstrahlung) and since their energy changes continuosly, the spectrum of braking radiation is also continuos.

The discrete part of the X-ray spectrum is a byproduct of the generation of SE electrons. When an atom is ionised, an electron from a higher energy level fills the emptied lower energy level to minimize the atom's energy, and again to make up for the change in energy, a photon, with energy equal to the difference of energies of the intial and final energy level, is emitted. However this time, since

the energy levels in the atom's orbit are discrete, the spectrum is also discrete. Because the orbital structure is unique for every element, we call the discrete part of the spectrum characteristic and it allows us to identify elements in a given material. Analysis of the discrete spectrum is the principle of EDX. The qualitative analysis then consists of matching the positions of spectral lines of the material with known spectral lines of individual elements.

In reality the detected spectra are not exactly discrete, but are made up of characteristic peaks. The intensity is affected by the concentration of a given element, allowing us to perform quantitative analysis. However the data can be influenced by numerous processes, thus several corrections need to be introduced. These effects include absorption, avalanche ionization and fluorescence [12].

In present thesis, the Brunker AXS EDX detector has been used together with the analysis software Esprit (see `https://www.bruker.com/en.html`), which includes, among others, the aforementioned corrections. EDX detectors are only able to detect energies higher than 100 eV and thus usually cannot detect elements lighter than boron. Detection of other light elements (namely, for the present work relevant oxygen) is problematic as well. That is, used EDX technique does not allow us to precisely determine the content of light elements in the sample.

The basic principle of an EDX detector is as follows: an X-ray photon hits the detector, usually a semi-conductor metal such as sillicone, generating an electron-hole pair, which are then attracted to opposite sides of the detector due to an applied voltage and thus a current pulse is generated. The pulse's magnitude is proportional to the photon's energy.

2.4 Magnetization Measurement

Magnetization of a material can be measured using various methods depending on the field strength and method accuracy. Magnetic field measurement devices are divided into two main categories depending on the field strength, in which the measured sample is investigated. For weak fields ($\mu_0 H < 1$ mT), magnetometers are used; for strong fields ($\mu_0 H > 1$ mT) gaussmeters are employed [13]. In present thesis, high-resolution superconducting quantum interference device (SQUID) has been deemed the most beneficial.

The SQUID magnetometer takes advantage of the so-called Josephson effect, where electrons penetrate an insulating barrier between two superconductors [14].
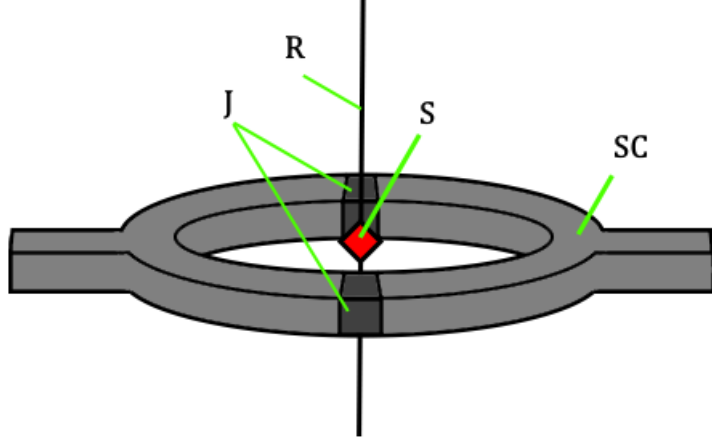
Figure 2.3: Diagram of a SQUID magnetometer. R - rod; SC - superconductor; J - Josephson junction; S - sample.

Placing a thin ($\sim$1 nm) insulating layer between two superconductors, forming a Josephson junction, allows the measurement of small changes in a magnetic field (10^{-9} - 10^{-1} mT) [13]. The Josephson effect is utilized in devices of two general types, DC and AC [15]. In the case of the $A_2Ir_2O_7$ pyrochlores, investigated in present thesis, we employed the DC SQUID, which incorporates the DC Josephson effect.

Generally the setup of a DC SQUID, as shown in Figure 2.3, consists of a superconducting ring with two Josephson junctions and a rod, which moves up and down, perpendicular to the ring's plane. The sample is attached to the rod, allowing it to pass through the ring, leading to an induced current proportional to the sample's magnetization [5]. The ring and the sample are placed in a cryogenic chamber, where the temperature is controlled generally by cryogenic liquids.

Due to the small size of the investigated samples ($\sim$100-500 μm), the reciprocating sample option (RSO) has been used. RSO allows higher resolution measurements by moving the sample periodically in the vertical direction respective to the ring's plane with an oscillation amplitude of $\sim$cm and frequency of $\sim$Hz [16].

3. Previous Results

The $A_2B_2O_7$ pyrochlores, where A represents a rare-earth element (generally elements with $5d$ and $4f$ electron configurations) and B represents the d transition metals or p elements, make up a wide group of materials studied for their complex and exotic phases and potential new physics [1, 6, 17]. In the present thesis we focus on rare-earth iridates, $B = $ Ir, with configuration $5d^7$.

The pyrochlore iridates have been found to crystallize in the cubic $Fd\bar{3}m$ space group no. 227. The lattice parameter a in these compounds varies between 10.1 - 10.4 Å. Ir atoms occupy the $16c$ and A atoms the $16d$ Wyckoff positions, individually forming corner-sharing tetrahedra which interpenetrate each other. The O ions occupy the $48f$ and $8b$ Wyckoff positions forming octahedra around the Ir atoms and cubes around the A atoms. As the $48f$ oxygen has one fraction

(a) (b)

(c) (d) (e)
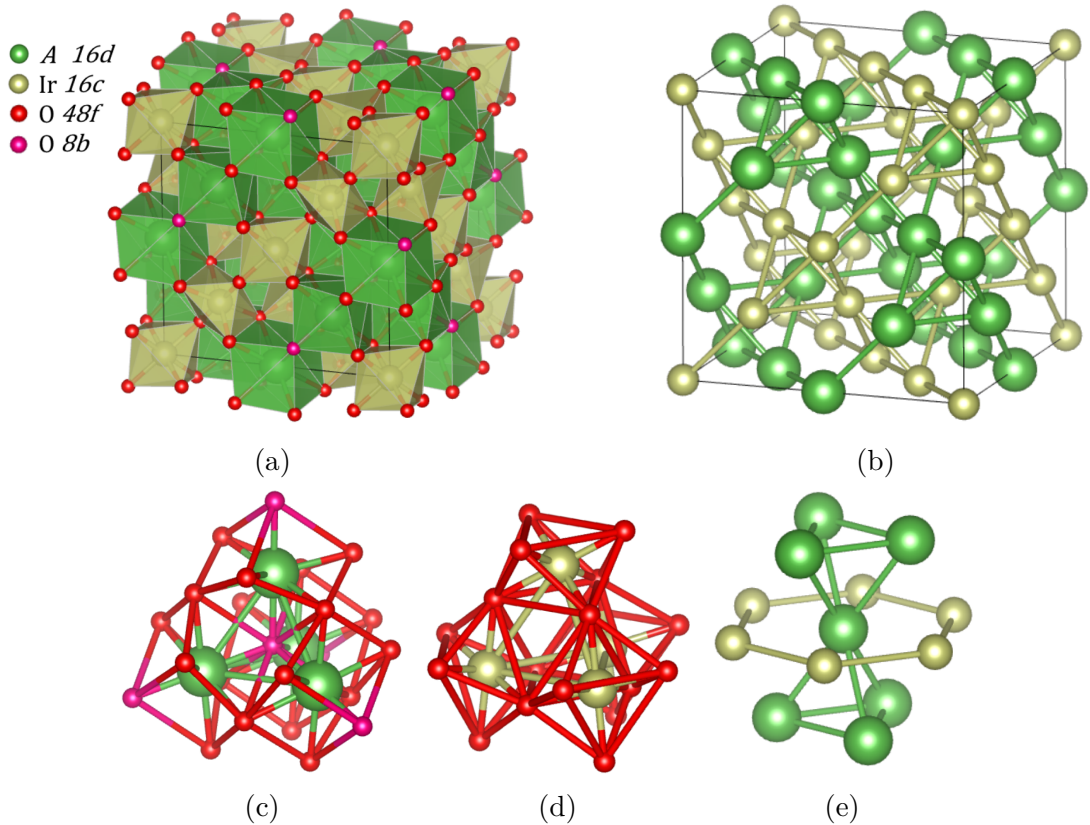
Figure 3.1: Pyrochlore iridate primitive lattice: (a) Primitive lattice highlighting the compressed O cages around A and Ir atoms; (b) Primitive lattice without O atoms highlighting the A and Ir interpenetrating tetrahedra by including virtual A-A and Ir-Ir bonds; (c) 4 edge-sharing O cubes around an A tetrahedron; (d) 4 edge-sharing O octahedra around an Ir tetrahedron; (e) Ir hexagon formed around two corner-sharing A tetrahedra.
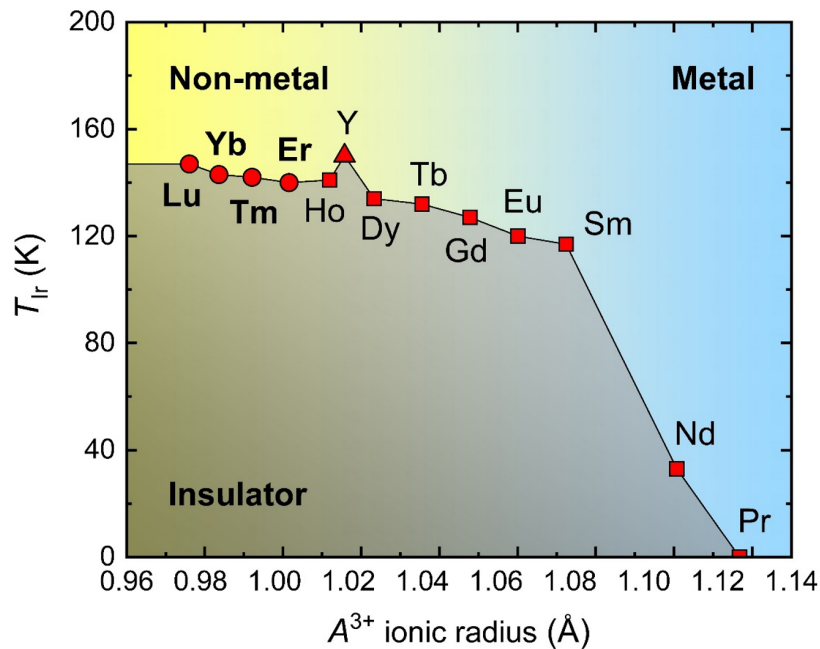
Figure 3.2: Temperature of metal-insulator transition/magnetic order as a function of the ionic radius of rare-earth elements [19].

coordinate free, the oxygen cages are not regular. They have been experimentally shown to be always trigonally compressed (either elongated or compressed along the [111] direction) [1, 18]. The primitive cell is shown in its entirety in Figure 3.1, including bonding O ions outside of the primitive cell. Oxygen cages are highlighted in Figures 3.1a, 3.1c and 3.1d. Only the Ir and A tetrahedra are depicted in Figure 3.1b. Furthermore, when we consider an A (or Ir) atom and the two tetrahedra it connects, a hexagon formed by Ir (or A) atoms in the (111) plane can be seen, as shown in Figure 3.1e.

While according to Hund's rules the Ir ions should carry a total angular momentum $J = 5/2$, the octahedral configuration of the O atoms causes splitting of the $5d$ orbital (creating the e_g and t_{2g} orbitals, described in a more general case in [5], for the case of iridates in [6]). It is then beneficial for the electrons to arrange themselves so that the Ir ions carry an effective angular momentum $J_{\text{eff}} = 1/2$.

Geometrical frustration, as introduced in section 1.3, in combination with the A-Ir exchange interactions and the crystal field (around the A and Ir atoms largely determined by the O atoms) determine the material's properties. The Ir-Ir interactions have been observed as the strongest and the A-A and A-Ir interactions are, for the most part of the $A_2Ir_2O_7$ series, relatively weak, at least at high temperature [1]. Of course there are exceptions, such as the case of $Pr_2Ir_2O_7$
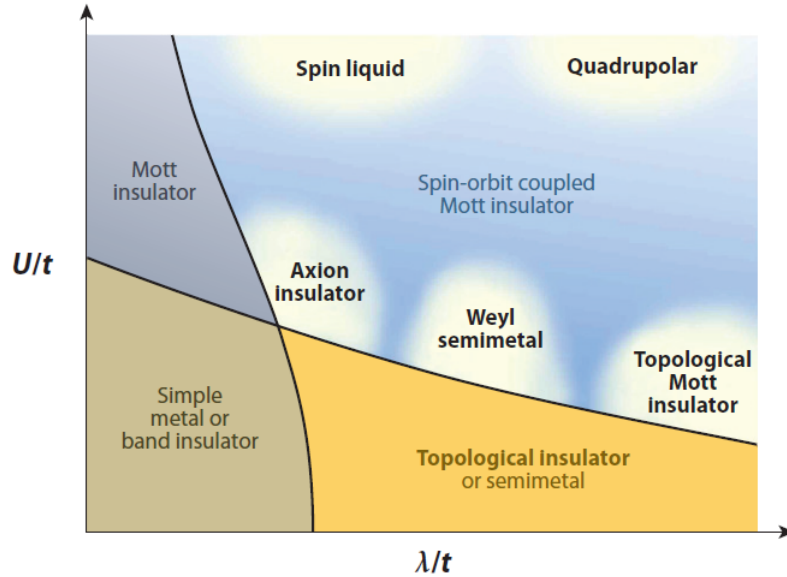
Figure 3.3: Phase diagram of exotic states based on the relative effects of SOC (described by the coefficient λ from equation 1.6) and electron correlations (Hubbard repulsion U), where t is the hopping amplitude [1].

discussed in [1] or strong coupling between A and Ir sublattices in $Tb_2Ir_2O_7$ [20]. Usually, there are two phase transitions in $A_2Ir_2O_7$ (e.g. observed for $Nd_2Ir_2O_7$ [21]). However for rare-earths, T_c is much lower than that of Ir.

One of the major experimental observations is the metal-insulator-transition (MIT) - a phase transition at the critical temperature T_c, caused by ordering of magnetic moments as presented in section 1.3. MIT corresponds to the magnetic ordering of one of the sub-lattices, the Ir sublattice. T_c of the Ir sublattice - T_{Ir} varies depending on the ionic radius of the A ion. In Figure 3.2, T_{Ir} is presented as a function of the atomic radius of rare-earth elements. This phase transition then carries over to the measurement of a number of properties such as response to an external magnetic field, resistivity or thermal conductivity; see e.g. [19, 22, 23].

Two of the most prominent interactions of the $5d$ ions are the SOC and electron correlations. As shown in Figure 3.3, a phase diagram can be drawn in terms of the relative strenght of the two interactions described by the coefficients λ (coefficient from equation 1.6), U (Hubbard repulsion - on-site interaction of electrons) and the hopping amplitude t (describing the hopping/tunneling of electrons between atomic sites) which appear in the generic model Hamiltonian [1, 6].

The Ir site ordering has been experimentally shown to be antiferromagnetic - Ir ions arrange themselves in the AIAO configuration [22], see Figure 1.2. While above T_{Ir}, the iridates generally exhibit paramagnetic behavior, below T_{Ir}, they order magnetically and a range of exotic phases have been either experimentally

confirmed or proposed [1, 17]. So-called spin ice state, the state when two magnetic moments point in and two out of the Ir (or A) tetrahedron, can be realized, and excited to the three in and one out state (Figure 1.2). Or the spin-liquid state with no long-range ordering can be introduced [1].

Even though the study of $A_2Ir_2O_7$ crystals continues to show promising results in exploring yet to be fully understood physics, their preparation has proven to be challenging as few studies have been conducted on usually off-stoichiometric single crystals [23, 24, 25]. In the present thesis we target the synthesis of $A_2Ir_2O_7$ single crystals, as well as their characterization and magnetic properties.

4. Results

The chapter consists of the specifics of our method of single crystal synthesis generally described in section 2.1 and results of measurements conducted on synthesized single crystals of $Lu_2Ir_2O_7$. Lutetium is of particular interest thanks to its atom structure. As for most rare-earths, Hund's rules serve as an accurate model [5] and Lu takes on the configuration $[Xe]6s^24f^{14}5d^1$. However in the crystal lattice it appears in the ionic state Lu^{3+} with the configuration $[Xe]4f^{14}$, therefore carries a zero magnetic moment. Response of $Lu_2Ir_2O_7$ to an external magnetic field is then dictated only by the magnetic Ir sublattice. $Lu_2Ir_2O_7$ thus allows us to study the magnetic properties of only the Ir sublattice, presumably generalizable to other $A_2Ir_2O_7$ members.

4.1 Preparation of $Lu_2Ir_2O_7$ Single Crystals

For the synthesis of $Lu_2Ir_2O_7$ single crystals, we have employed the flux method described in section 2.1, as it had been deemed the most appropriate after comparison with other methods [10].

The intial stoichiometric mixture of reactans consisted of 99.99 % (AlfaAesar) pure oxides Lu_2O_3 and IrO_2, as well as lead fluoride, serving as flux in a 1:60 (material:flux) ratio, all in powder form. In Figure 4.1a, the setup for preparation of the initial mixture is shown. Using an agate mortar and a pestle, the oxides were ground into a homogenous mixture. The total mixture was then
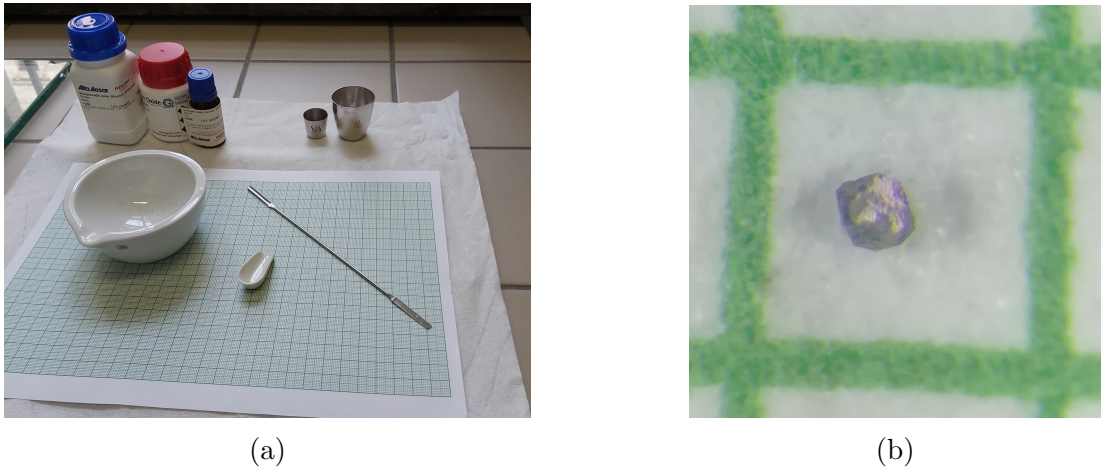

(a)	(b)

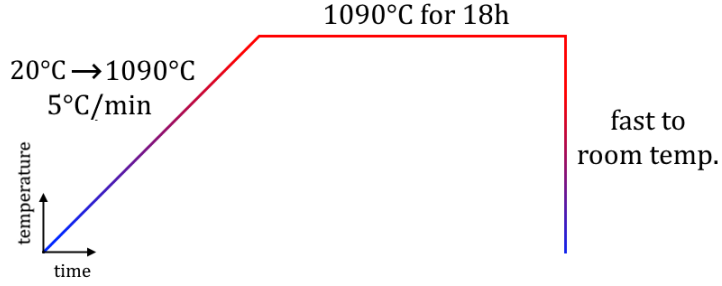Figure 4.1: (a) Photograph of the intial mixture preparation setup; (b) Picture of $Lu_2Ir_2O_7$ taken using a camera connected to an optical microscope.

Figure 4.2: Diagram of the heating profile used for $Lu_2Ir_2O_7$ synthesis

placed into an open platinum crucible together with the flux and subsequently heated in a resistance furnace. Choosing an optimal heating profile has been found to be complicated due to evaporation of IrO_2 at relatively low temperatures ($\sim$1000-1200°C [10]). After numerous attempts with varying mixture-flux ratio, maximum temperature and time duration, the heating profile depicted in Figure 4.2 had been determined to be optimal. The mixture was heated from room temperature to 1090°C at a rate of 5°C/min and after 18 hours at 1090°C, the sample was cooled down to room temperature. The process allowed maximizing flux evaporation, while minimizing material evaporation, in turn allowing maximum size and phase purity using the flux method.

Our method resulted in octahedron-shaped bi-pyramid single crystals in a thin layer of solidified flux. A picture from an optical microscope of a synthesized single crystal is presented in Figure 4.1b. The maximum crystal sizes ranged between 100-500 μm.

4.2 Characterization

Synthesized $Lu_2Ir_2O_7$ single crystals were investigated by means of Laue diffraction and SEM described in sections 2.2 and 2.3, respectively.

Although due to the small size of the samples the process of orienting the crystals in the diffractometer had been difficult, we successfully recorded the diffraction pattern presented in Figure 4.3. In said diffractogram, we see either a three-fold or a six-fold symmetry. Considering the crystal shape, we can eliminate six-fold symmetry and we can thus deduce that the reflection maxima correspond to the (111) plane. The seemingly six-fold symmetry could also be caused by a second grain or a mosaicity, however such ocurrences would not affect our measurements. The obtained diffractogram thus confirms the predicted cubic structure of the samples.
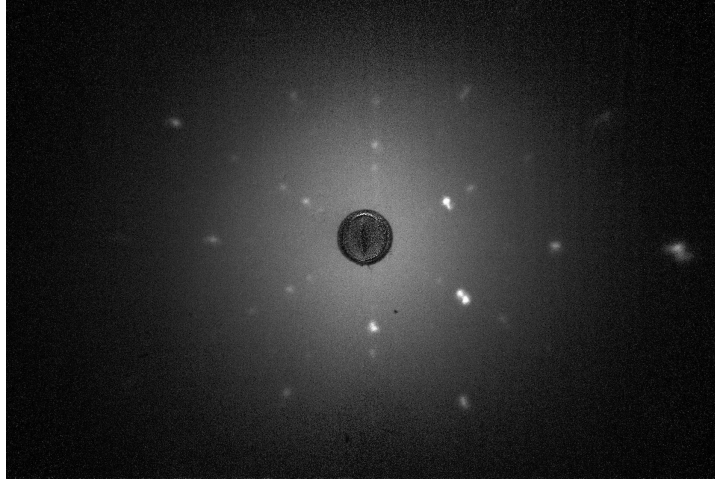
Figure 4.3: X-ray diffraction pattern of an $Lu_2Ir_2O_7$ single crystal obtained by means of Laue diffraction method.

The SEM allowed us to obtain high resolution images of the prepared single crystals presented in Figure 4.4. The images were processed using the BSE mode, i.e. detection of back scattered electrons as described in section 2.3. Generally the crystals exhibit the bi-pyramid (octahedron) shape expected for the $A_2Ir_2O_7$ family with relatively smooth facets indicating a single crystal structure. Even though the crystals can grow seperately, such as the two presented in Figure 4.4a and 4.4c, they can also grow in clusters , like the ones in Figure 4.4b and 4.4d. For measurements reliant on the single-crystalline structure (Laue diffraction, magnetization measurement discussed in the following section), the isolated crystals are more desirable, since clusters imply the possibility of multiple lattice orientations, as can be seen in the cluster in Figure 4.4d, where it is especially prominent. We may also notice certain imperfections which stem from the growth method such as the rough surface of the sample in Figure 4.4c, which is in fact a thin layer of flux, also present to a lesser extent on the other samples. Before the synthesized samples were investigated by magnetization measurement, the flux layer was mechanically removed.

As mentioned in section 2.3, the SEM employed in the present thesis also includes an EDX detector. Using the analysis software Esprit, we were able to determine the relative concentrations of Lu and Ir. As mentioned in section 2.3, EDX cannot offer meaningful data for light elements, therefore the concentration of O cannot be determined. The mass ratio Lu:Ir was calculated as $51(\pm1){:}49(\pm1)$. Measurements also showed high concentrations of lead in samples with a rough surface, such as the one pointed out in the previous paragraph, indicating an elevated presence of the employed flux on the given surface.
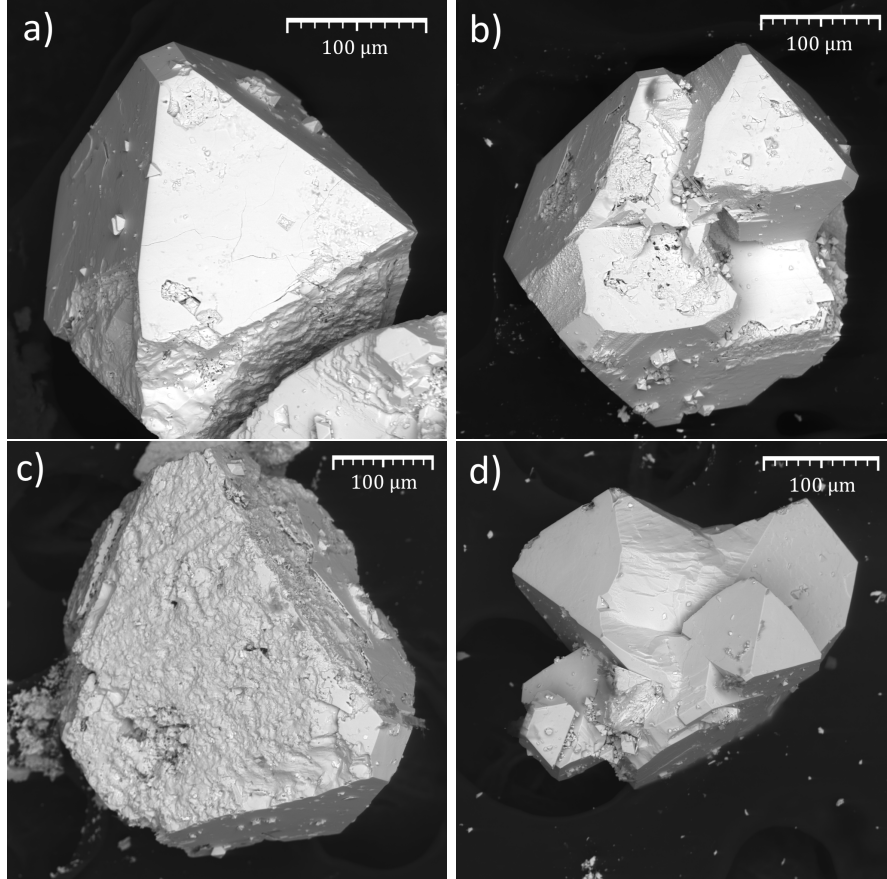
Figure 4.4: Images of $Lu_2Ir_2O_7$ single crystals obtained using SEM in the BSE mode.

4.3 Magnetic Properties

In this section, we focus on the magnetic measurements on the synthesized and characterized $Lu_2Ir_2O_7$ single crystals. Evolution of magnetization with temperature and external magnetic field was investigated using the SQUID magnetization measurement device with the RSO option described in section 2.4. The measurement of single crystals allowed us to investigate anisotropy effects in the material. Measurements were performed along the principal crystallographic directions [100], [110] and [111], which on the macroscopic scale of the sample correspond to the directions drawn in Figure 4.5 (i.e. we measured the magnetization with field applied in the direction of the drawn arrows).

The temperature of magnetic ordering was investigated on $Lu_2Ir_2O_7$ single crystals for the first time. The magnetization was measured under the zero-field-cooled and field-cooled (ZFC and FC) regimes: from room temperature ($\sim$300 K) down to 2 K in zero magnetic field, then the magnetic field was turned on and the magnetization was measured while increasing the temperature. Since the sample
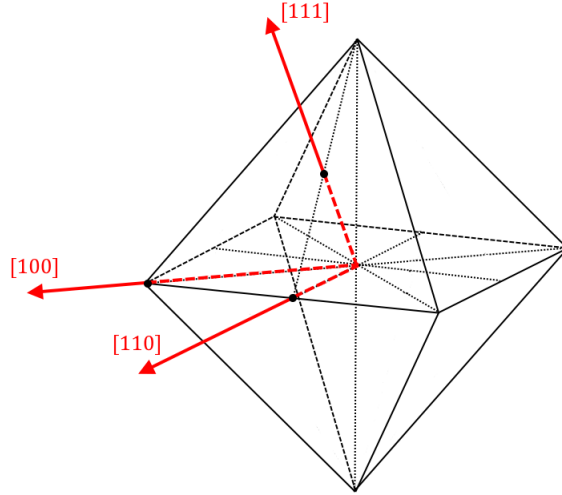
Figure 4.5: Principal crystallographic directions of a cubic lattice shown on an octahedron simulating the synthesized samples. These directions were chosen for measurement of anisotropy effects in $Lu_2Ir_2O_7$ single crystals.

is cooled without the presence of a magnetic field, this measurement is referred to as zero-field-cooled (ZFC). Without changing the magnetic field, we repeat the process. Because the sample is cooled in the presence of a magnetic field, the process is referred to as field-cooled (FC). Diagrams of the individual processes are drawn in the inset of Figure 4.6. For a material which magnetically orders, a bifurcation between ZFC and FC is expected at/below the critical temperature T_c.

When the sample is cooled in zero magnetic field, the magnetic moments order below T_c and after a magnetic field is applied, they tilt (slightly) depending on the direction of the magnetic field, resulting in a strong net magnetization relative to the paramagnetic state (regardless of the type of ordering, which is why this method only allows us to determine T_c, not the type of magnetic ordering; although ferromagnetic order leads to non-zero net magnetization even without applied magnetic field). In an ideal antiferromagnet/ferromagnet, the FC process would be no different from ZFC, however in reality, not all the magnetic moments arrange themselves in the given configuration. The applied magnetic field could overpower some of the fluctuations, resulting in e.g. alignement of moments along the field and a higher magnetization. Hence the bifurcation between ZFC and FC magnetizations is observed. In the paramagnetic state, the thermal fluctuations become stronger than the exchange interactions and the magnetization becomes dependant only on the external magnetic field.

In Figure 4.6, the ZFC and FC magnetization measurements with applied
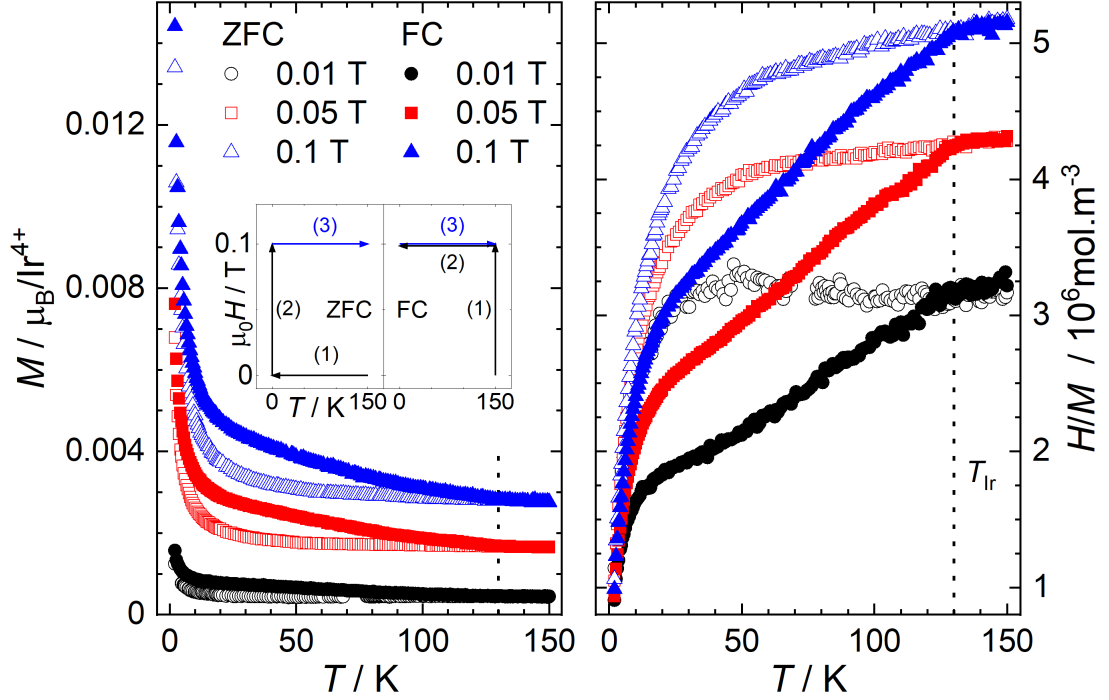
Figure 4.6: Magnetization measurements under ZFC and FC regimes as functions of temperature with magnetic field applied along the [111] direction. The ordering temperature denoted by the dotted line in both panels has been determined to be $T_{\text{Ir}} = 130(1)$ K. Inset: Diagram of the ZFC and FC regimes respectively; ZFC: (1) sample is cooled, (2) magnetic field is introduced, (3) measurement of magnetization with increasing temperature in a magnetic field is performed; FC: (1) magnetic field is introduced, (2) sample is cooled, (3) measurement of magnetization with increasing temperature in a magnetic field is done.

magnetic field $\mu_0 H = 0.01$ T, 0.05 T, and 0.1 T along the direction [111] are presented. A clear bifurcation at the critical temperature $T_{\text{Ir}} = 130(1)$ K, denoted by the dotted lines, has been observed. The difference between ZFC and FC magnetizations becomes more pronounced the higher the external magnetic field is, as more fluctuations are suppressed by it. The bifurcation is even more pronounced when we calculate the inverse susceptibility, i.e. the reciprocal of the magnetization divided by the magnetic field, H/M. We also point out the fact that the ZFC magnetization is strictly convex, i.e. there is no dip in M below T_{Ir}, as opposed to measurements for some of the other rare-earth iridates (e.g. $Er_2Ir_2O_7$ and $Yb_2Ir_2O_7$ in [19]), for which the magnetization decreases below the value of the paramagnetic state before diverging at much lower temperature.

Similar evolution of magnetization was observed for magnetic field applied along other crystallographic directions, for $\mu_0 H = 0.1$ T, we compare M and H/M for the crystallographic directions [100], [110] and [111] in Figure 4.7. In
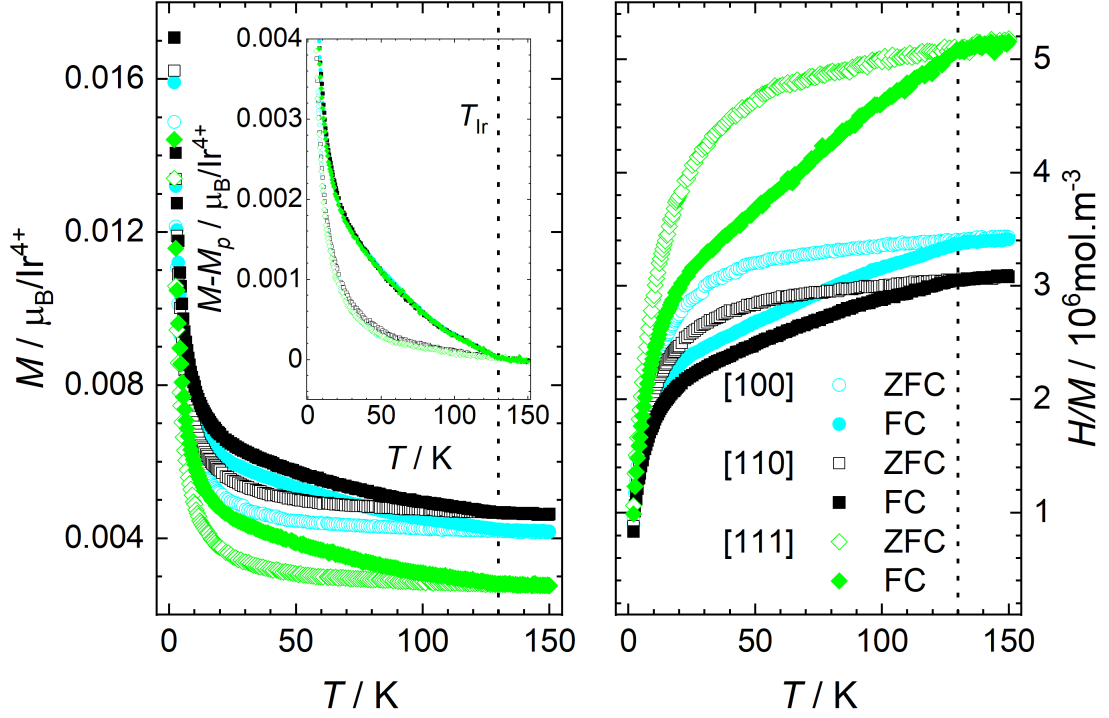
Figure 4.7: Magnetization measurements under ZFC and FC regimes for magnetic field $\mu_0 H = 0.1$ T applied along the crystallographic directions [100], [110] and [111]. Critical temperature T_{Ir} is denoted by the dotted line. Inset: Magnetization with the paramagnetic magnetization M_p subtracted.

the inset, we subtracted from the measured magnetization its mean value for $T > T_{Ir}$ denoted M_p for paramagnetic magnetization. Near 2 K, the response to a magnetic field appears to be almost isotropic. At higher temperature, generally M is largest with magnetic field applied along the direction [110], with [100] only slightly lower, and lowest in the direction [111]. This is further demonstrated on isothermal magnetization in Figure 4.8 discussed below. From the inset we can see that the curves are almost identical after subtracting the constant "paramagnetic" signal.

We also note that in Ref. [2], a bifurcation between ZFC and FC magnetizations below 140 K has been observed in a polycrystalline $Lu_2Ir_2O_7$. Despite the difference in the measured T_{Ir}, the two works, on poly- and single crystals, are in good agreement. Lower T_{Ir} in the single crystal could be ascribed to slight off-stoichiometry (used electron microscope with EDX analyser is not sufficiently sensitive to oxygen content) or even admixture of Ir^{5+} as speculated about in the powder sample [2].

Next we investigate the response to a varying external magnetic field at 2 K, 20 K and 90 K. Magnetization measurement was done on samples cooled down to
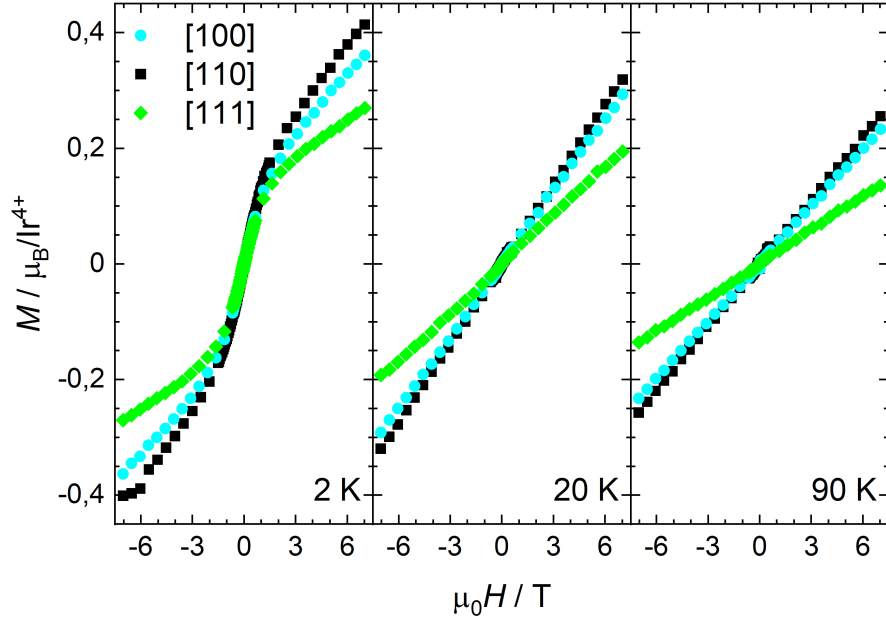
Figure 4.8: Isothermal magnetization (ZFC sample before measurement) of $Lu_2Ir_2O_7$ with an external magnetic field along the principle crystallographic directions [100], [110] and [111] for 2 K, 20 K and 90 K. Only measurement from 7 T to -7 T is presented (other measurements overlap as discussed in text).

a selected temperature under following regimes: without a magnetic field - ZFC, in the presence of a 7 T magnetic field - 7TFC, and a 7 T field in the opposite direction - -7TFC. Once the selected temperature was reached, measurements were performed while varying the magnetic field from 0 T up to 7 T, then from 7 T down to -7 T and lastly from -7 T back to 0 T. In Figure 4.8, we present the ZFC magnetization from 7 T to -7 T for the three crystallographic directions. The overall field dependance of magnetization seems to be unchanged for the three directions. For stronger magnetic fields the magnetization measured (in absolute value) in the [111] direction is smaller than in [100] and [110], which are relatively close to each other. Similar effect was accordingly observed in Figure 4.7 for temperature dependencies.

Magnetization data measured with the magnetic field applied along the crystallographic direction [111] are presented in Figure 4.9. First, on the left hand side panel of Figure 4.9 are presented the ZFC measurements for 2 K, 20 K and 90 K. We note that there is no hysteresis. Absence of hysteresis in magnetization data is indicative of an antiferromagnetic ordering as theorized for the Ir^{4+} sublattice (AIAO, Figure 1.2 in section 1.3, [1]). The measurements at higher temperatures 20 K and 90 K are shown from 7 T to -7 T only. For higher temperatures (although below $T_{Ir} = 130(1)$ K) the field dependence of magnetization appears
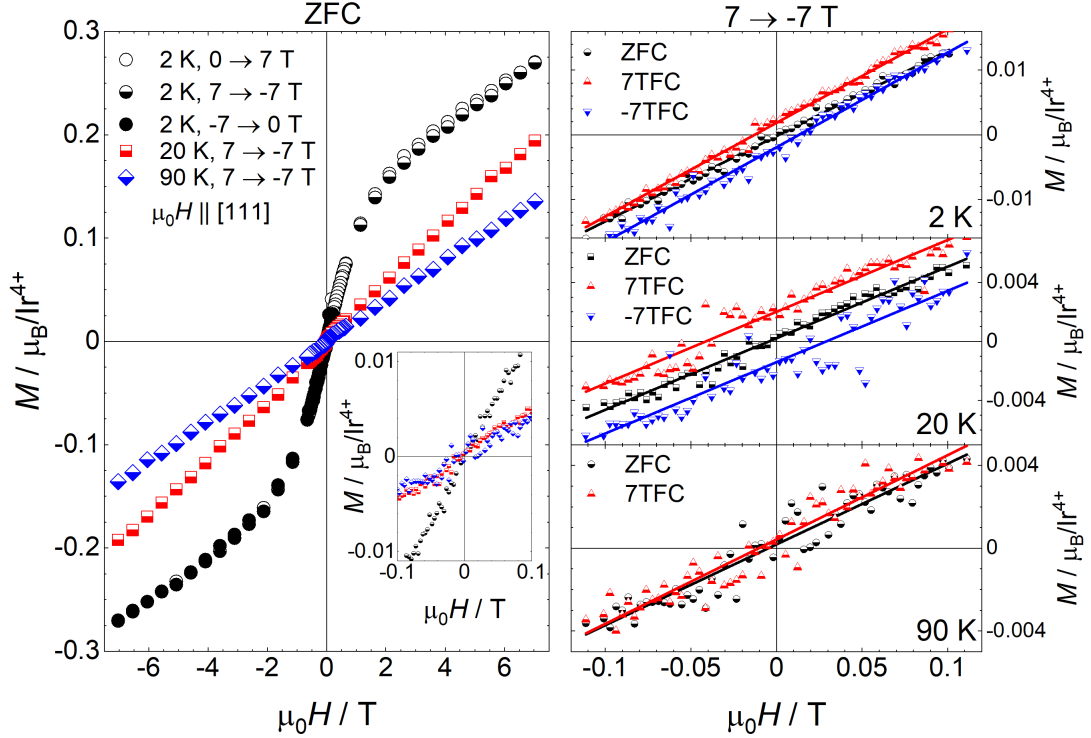
27

Figure 4.9: Magnetization response to an external magnetic field applied along the [111] direction at temperatures 2 K, 20 K and 90 K. For each temperature ZFC, 7TFC and -7TFC measurements were performed, i.e. cooling with no field (ZFC), in a 7 T field (7TFC) and in a 7 T field in the opposite direction (-7TFC). Each measurement consisted of varying the field from 0 T to 7 T, from 7 T to -7 T and from -7 T back to 0 T. Data on the right hand side are linearly fitted between -0.12 T and 0.12 T to better express general trends.

almost linear, while for 2 K the data are clearly non-linear and appear to tend towards a saturated value. The saturation is, however, not reached in applied field up to 7 T, and presumably will not be reached up to significantly higher field. Theoretical value of saturated magnetization for an Ir^{4+} free ion in the spin-$\frac{1}{2}$ state is $1.73\mu_B$ [2]. Therefore the magnetization of $Lu_2Ir_2O_7$ is expected to increase substantially by application of a higher magnetic field.

Second, on the right hand side of Figure 4.9, we see the ZFC, 7TFC and -7TFC measurements around $\mu_0H = 0$ T. At 2 K and 20 K, ZFC gives $M \approx 0$ at $\mu_0H = 0$ T, while 7TFC data show $M > 0$ and similarly -7TFC regime leads to $M < 0$. At 90 K, magnetization is approximately the same for both ZFC and 7TFC. Importantly, $Lu_2Ir_2O_7$ magnetically orders below 130 K as illustrated in Figure 4.6. No difference between ZFC and 7TFC curves at 90 K and clear difference at lower temperature indicates stronger response, that is, stronger magnetic moment/exchange between Ir ions, at low temperature. The data at small fields,

between -0.12 T and 0.12 T were linearly fitted to quantify the signal, i.e. calculate the intersection point of $M(H)$ with the y-axis. Supposing that it is zero for ZFC, it can be approximated by taking the mean of the values for 7TFC and -7TFC. We obtain $0.0019\ \mu_B/\mathrm{Ir}^{4+}$ at 2 K and $0.0017\ \mu_B/\mathrm{Ir}^{4+}$ at 20 K. Although two values are not enough data to form a conclusion, we expect the difference to decrease with increasing temperature. Higher temperature implies more thermal fluctuations.

Offsets observed in the low temperature ± 7TFC regimes, relative to the ZFC regime, can be explained by formation of domain walls between the antiferromagnetic Ir domains. In the ZFC regime, the Ir magnetic moments order almost homogeneously in the AIAO configuration, forming randomly oriented domains of AIAO and AOAI. When a magnetic field is applied during cooling through T_{Ir}, the configuration of the moments, domains and domain walls are affected. The Ir sublattice then settles into a new favorable energy state containing antiferromagnetic domains separated by field oriented domain walls, which have a non-zero net magnetic moment and can be therefore considered ferromagnetic [26]. Since the domain walls are ferromagnetic and the offset is roughly constant across the entire sweep cycle, we can infer that the deformation is permanent/the domain structure is robust against external variables, unless temperature increases above T_{Ir}.

The study of formation and stability of these ferromagnetic interfaces represents a very topical subject of research in pyrochlore iridates as prospective materials for spintronic applications. Once the antiferromagnetic domains and ferromagnetic interfaces are stabilized by magnetic field crossing the T_{Ir}, while the field in order of mT is sufficient to stabilize the structure [unpublished research at DCMP], the interfaces are robust against an applied field of, at least, 7 T. This makes these materials ideal magnetic recording media. Simultaneously, the conductivity of domains (Mott insulator) and interfaces (high metalic conductivity) significantly differ. This could be used to read magnetically encoded information by an external electric field. These properties and mechanisms have not been fully proven by microscopic studies due to lack of good-quality materials. Further studies on, in this thesis synthesized, $\mathrm{Lu_2Ir_2O_7}$ singles crystals are envisaged in the very near future in the frame of broader research at DCMP.

Conclusion

For the first time, stoichiometric $Lu_2Ir_2O_7$ single crystals have been successfully synthesized by the flux method. The non-magnetic rare-earth sublattice with Lu^{3+} ions allowed the study of magnetic properties of the isolated Ir sublattice.

Measurements of magnetization with temperature under the ZFC and FC regimes exhibit a bifurcation at the temperature $T_{Ir} = 130(1)$ K in $Lu_2Ir_2O_7$, thus evidencing the ordering of the Ir sublattice at this critical temperature. The measurements were performed with magnetic field applied along the principal crystallographic directions [100], [110] and [111]. Weak anisotropy between [100] and [110] directions was observed, while magnetization along the [111] direction differs considerably. This anisotropy is better illustrated in isothermal magnetization data measured with field applied along the three principal directions.

Magnetization response to a magnetic field in $Lu_2Ir_2O_7$ under ZFC and FC regimes at constant temperature below T_{Ir} displays an absence of hysteresis, indicating rather antiferromagnetic ordering of the Ir sublattice, further supported by the absence of remanent magnetization under the ZFC regime. Under the FC regimes, a constant offset in the magnetization along the direction of the applied field has been observed at temperatures 2 K and 20 K, which could be explained by the proposed formation of antiferromagnetic domains and ferromagnetic domain walls. The domain walls bear a non-zero net magnetization which is strongly influenced by the applied magnetic field, that is, ferromagnetic moments are oriented in the field direction leading to observed offset in magnetization data.

In summary, $Lu_2Ir_2O_7$ single crystals display promising magnetic properties for applications in spintronics. The ability to induce ferromagnetic moments (in domain walls) by mT fields, which are resilient to fields of up to 7 T, gives the $A_2Ir_2O_7$ materials the potential to be used for magnetic recording. However, further research into these materials is warranted to confirm the discussed properties. At Charles University's Department of Condensed Matter Physics, study of the $A_2Ir_2O_7$ pyrochlores is ongoing. The flux method described in present thesis has been found applicable to other pyrochlore iridates (not discussed in this thesis). In the near future synthesized single crystals of other members of the pyrochlore iridates will allow to properly investigate their complex electronic and magnetic properties. The presented results on $Lu_2Ir_2O_7$ with pure (rare-earth magnetism free) Ir magnetism will be heavily utilized to interpret these complex properties.

Bibliography

[1] Witczak-Krempa W., Chen G., Kim Y. B., Balents L. Correlated Quantum Phenomena in the Strong Spin-Orbit Regime. *Annual Reviews*, 2014.

[2] Klicpera M., Vlášková K., Diviš M. Low-temperature properties of pyrochlore $Lu_2Ir_2O_7$. *Journal of Magnetism and Magnetic Materials*, 2020.

[3] Sedlák B., Štoll I. *Elektřina a magnetismus.* Druhé opravené vydání. Academia, Praha, 2002.

[4] Feynman R., Leighton R., Sands M. *The Feynman Lectures on Physics.* New Millennium edition. Basic Books, New York, 2011.

[5] Blundell S. *Magnetism in condensed matter.* Oxford University Press Inc., New York, 2001.

[6] Lefrançois E. *Synthesis and study of iridium oxide compounds for entangled spin-orbit physics.* PhD thesis, l'École doctorale de Physique de Grenoble, 2016.

[7] Daniš S. *Atomová fyzika a elektronová struktura látek.* Vydání první. matfyzpress, Praha, 2019.

[8] Abendschein A., Capponi S. Effective Theory of Magnetization Plateaux in the Shastry-Sutherland Lattice. *Physical Review Letters*, 2008.

[9] Callen H. *Thermodynaics and an introduction to thermostatistics.* Second edition. Wiley, New Jersey, 1991.

[10] Vlášková K., Colman R. H., Klicpera M. Synthesis of $Er_2Ir_2O_7$ pyrochlore iridate by solid-state-reaction and CsCl flux method. *Materials Chemistry and Physics*, 2021.

[11] Müller G. Fundamentals of Melt Growth. In *AIP Conference Proceedings 916, 3-33*, 2007.

[12] Belk J. A. *Electron Microscopy and Microanalysis of Crystalline Materials.* Applied Science Publishers LTD, London, 1979.

[13] Macintyre S. A. *Magnetic Field Measurement.* CRC Press, 2000. Section 48. of *The Measurement, Instrumentation and Sensors Handbook*.

[14] Ibach H., Luth H. *Solid State Physics.* Springer, Berlin, Heidelberg, 2009.

[15] Ryu C., Blackburn P. W., Blinova A. A., Boshier M. G. Experimental Realization of Josephson Junctions for an Atom SQUID. *Physical Review Letters*, 2013.

[16] Sawicki M., Stefanowicz W., Ney A. Sensitive SQUID magnetometry for studying nanomagnetism. *Semiconductor Science and Technology*, 2011.

[17] Rau J. G., Lee E. K.-H., Kee H.-Y. Spin-Orbit Physics Giving Rise to Novel Phases in Correlated Systems: Iridates and Related Materials. *Annual Reviews*, 2016.

[18] Lefrançois E., Simonet V., Ballou R. et al. Anisotropy-Tuned Magnetic Order in Pyrochlore Iridates. *Physical Review Letters*, 2015.

[19] Klicpera M., Vlášková K., Diviš M. Characterization and Magnetic Properties of Heavy Rare-Earth $A_2Ir_2O_7$ Pyrochlore Iridates, the Case of $Tm_2Ir_2O_7$. *The Journal of Physical Chemistry*, 2020.

[20] Guo H., Ritter C., Komarek A. C. Magnetic structure of $Tb_2Ir_2O_7$ determined by powder neutron diffraction. *Physical Review B*, 2017.

[21] Guo H., Ritter C., Komarek A. C. Direct determination of the spin structure of $Nd_2Ir_2O_7$ by means of neutron diffraction. *Physical Review B*, 2016.

[22] Jacobsen H., Dashwood D. D. et al. Strong quantum fluctuations from competition between magnetic phases in a pyrochlore iridate. *Physical Review Letters*, 2020.

[23] Tian Z., Kohama Y. et al. Field-induced quantum metal-insulator transition in the pyrochlore iridate $Nd_2Ir_2O_7$. *Nature Physics*, 2016.

[24] Donnerer C., Rahn M. C. et al. All-in-all-Out Magnetic Order and Propagating Spin Waves in $Sm_2Ir_2O_7$. *Physical Review Letters*, 2016.

[25] Ueda K., Fujioka J., Terakura C., Tokura Y. Pressure and magnetic field effects on metal-insulator transitions of bulk and domain wall states in pyrochlore iridates. *Physical Review B*, 2015.

[26] Pearce M.J., Götze K., et al. Magnetic monopole density and antiferromagnetic domain control in spin-ice iridates. *Nat Commun*, 2022.

List of Figures

List of Abbreviations

A ... rare-earth elemenent (Y, La-Lu)

$\vec{A}$ ... vector potential

AFM ... antiferromagnetic

AIAO ... all-in-all-out, arrangement of magnetic moments on a regular tetrahedron

AOAI ... all-out-all-in, arrangement of magnetic moments on a regular tetrahedron

B ... transition metal or p element

$\vec{B}$ ... magnetic induction

$\vec{B}_{hkl}$ ... reciprocal lattice vector

BSE ... back scattered electrons

$\vec{b}_{1,2,3}$ ... reciprocal basis vectors

χ ... magnetic susceptibility

DCMP ... Department of Condensed Matter Physics

E ... internal energy

EDX ... energy-dispersive X-ray

e ... elementary charge

FC ... field-cooled

G ... Gibbs free energy

g ... Landé g-factor

$\vec{H}$, H ... magnetic intensity

H_{SOC} ... hamiltonian term describing SOC

h, k, l ... Miller indices

I ... current

J, J_{eff} ... total angular momentum quantum number

$\vec{J}$ ... total angular momentum

$\vec{j}$ ... current density

λ ... SOC interaction coefficient

$\vec{L}$ ... orbital angular momentum

μ_0 ... vacuum permeability

$\vec{\mu}$ ... magnetic moment

$\vec{M}$, M ... magnetization

MGML ... Materials Growth and Measurement Laboratory

MIT ... metal-insulator transition

M_p ... paramagnetic magnetization

m ... mass

PE ... primary electrons

p ... pressure

$\vec{q}$ ... scattering vector

$\vec{R}$, R ... relative position vector

$\vec{r}$, r ... position vector

RKKY ... Ruderman-Kittel-Kasuya-Yosida

RSO ... reciprocating sample option

$\mathbf{\Sigma}$ ... surface

$\vec{\sigma}$ ... normal of a surface

S ... entropy

$\vec{S}$ ... spin

SE ... secondary electrons

SEM ... scanning electron microscope

SOC ... spin-orbital coupling

SQUID ... superconducting quantum interference device

T ... temperature

T_c (T_{Ir}) ... critical temperature (of Ir sublattice)

U ... Hubbard repulsion energy

V ... volume

ZFC ... zero-field-cooled

1I3O ... 1-in-3-out, arrangement of magnetic moments on a regular tetrahedron

2I2O ... 2-in-2-out, arrangement of magnetic moments on a regular tetrahedron

3I1O ... 3-in-1-out, arrangement of magnetic moments on a regular tetrahedron